Radiation from a Nongray Scattering, Emitting, and Absorbing Solid Rocket Motor Plume

D. K. Edwards* and D. S. Babikian†
University of California, Irvine, Irvine, California 92717

An engineering model of plume particulate radiation is extended to include nongray particles and gases. Optical constants of alumina with impurities are used to fix spectral variations of the alumina particulates. Soot particulate is similarly modeled. Parametric calculations are reported to show the influence of nongray behavior, gas-soot radiation, nozzle wall radiation, afterburning, small-particle and large-particle loadings, and particle heat transfer and optical property temperature variations. Gas and soot radiation are shown to have little influence upon solid rocket motor (SRM) plume radiation. Nozzle wall radiation is significant near the SRM exit if the nozzle wall temperature exceeds 1200 K. Afterburning has a large effect maintaining high-particle temperatures and high-plume intensity downstream of the exit. When the scattering optical depth due to small particles is large, directional variations in the plume boundary intensity are small, but not when the scattering optical depth is small. Particle cooling calculations indicate lower values of plume radiosity than are often observed, thus continuing the need for an engineering model based upon radiometic measurements. Suggestions are made for improving phenomenological models of SRM plume radiation.

Nomenclature

A_i = constants in Eq. (1)
B = Planck's function, W/m^2 cm^{-1}
B_i = constants in Eq. (1)
c = velocity of light, m/s
D = particle diameter, μm
D_0 = characteristic size of particle populations, μm
f = fraction
h = Planck's constant, Js
I = radiant intensity, W/m^2 sr
k = Boltzmann constant, J/K
K = extinction or (with subscript) absorption coefficient, m^{-1}
$\dot{m}$ = mass flow rate, kg/s
M = molecular weight
n = power law exponent; also Rosin-Rammler exponent, Eq. (9)
n_1 = refractive index
n_2 = absorptive index
P = pressure, atm
q = radiant flux, W/m^2
Q = efficiency factor based on geometric cross section
r = distance along a line of sight; also particle radius, μm
R = nozzle radius, m
t = optical depth
T = temperature, K
u = defined by Eq. (7d)
v = defined by Eq. (7e)
V = zone volume, m^3; also gas velocity, m/s
x = defined by Eq. (7b)
z = distance from the apex of the cone along its surface, m
Z^* = nondimensional value, $Z^* = z/R_e$
α = integrated band intensity, cm^{-1}/(g/m^2)
β = cone angle; also the phase angle defined by Eq. (7c)
γ = specific heat ratio
ε = electric constant, C^2/N m^2; also (with subscript) emissivity
θ = forward scattering angle, also angle from plume normal
λ = wavelength, μm
ν = wavenumber, cm^{-1}
π = 3.14159...
ρ = real parameter defined by Eq. (7a)
σ = electric conductivity of alumina, $(\Omega\text{m})^{-1}$
ϕ = azimuthal angle from upstream
ω = exponential bandwidth, cm^{-1}; also albedo of alumina

Subscripts

a, abs = absorption
c = cold particles; also center of a band
e = exit reference conditions
ex = extinction
g = gas
h = large hot particles
i = abs, ex, or pr
j = g, h, or sp
k = kth band
m = mass; also melting point
p = particles
pr = radiation pressure
s = soot
t = throat, also thermal blackbody emission
sp = small hot particles
v = volume
w = wall
0 = spectral reference condition

Introduction

RADIATION emitted by rocket motor plumes subjects aft-end equipment to heating loads and provides means for detection and diagnostics. The problem of modeling heating can be regarded as distinct from the problem of modeling plume signature because the former is more restricted both spatially and spectrally. Remote viewing of a plume's "signa-

---

Received Aug. 4, 1989; revision received Nov. 13, 1989. Copyright © 1990 by the American Institute of Aeronautics and Astronautics, Inc. All rights reserved.

*Professor of Mechanical Engineering. Fellow AIAA.

†Postgraduate Research Engineer. Student Member AIAA.

ture" may take in a spatial range of say 10^4 m, and, for detection and diagnostics, spectral features in selected wavelength bands may be emphasized in the detection optics. The signature problem takes in the far flow and any part of the entire spectrum from the ultraviolet to the far infrared but involves lines of sight that are essentially parallel in passing through the plume and that have essentially equal values of $1/r^2$. In contrast the aft-end equipment views the plume close in. Lines of sight have an appreciable range of directions and have greatly varying $1/r^2$ values along them. The plume immediately downstream of the thrust cone exit plane, approximately the first 10 m only, looms large in the heating problem, and the far plume is of secondary importance.

The signature problem with its obvious tactical value has received considerable attention during the past 40 years. Ludwig et al.[1] developed the standard infrared radiation model (SIRRM) code, which has been improved by Malkmus and colleagues[2,3] and used by Nelson[4,5] to examine the signature of plumes with particles in the 2–5 μm (5000–2000 cm^{-1}) spectral range. Nelson[5] concluded that alumina "is a weak absorber/emitter in the 2000–5000 cm^{-1} wave number band; consequently the source of the plume radiation is due to gas emission. Particle scattering influences the signature by changings its directional pattern." Lyons et al.[6,7] concentrated on the visible and near-ultraviolet spectral range with particular emphasis on near head-on angles of viewing. They concluded "...alumina particle radiation dominates through most of the visible region." They showed that afterburning in an atmospheric plume was important.

The heating problem, although of obvious engineering value, has received relatively little attention. In the case of metal-oxide-containing solid rocket motor (SRM) plumes, the Bobco[8] model has been used for the past 20 years. The near plume boundary is modeled as a solid, diffusely emitting surface of conical shape with axially varying radiosity. In this engineering model, three parameters—the cone half-angle, exit radiosity, and radiosity decay exponent—specify the plume well enough to permit the calculation of aft-end radiant heating. A video or photographic frame to show the angle and two narrow-angle radiometer readings, one a few centimeters aft of the exit and the other a meter or two aft, often are used to define the model. An alternative engineering model based upon volume emission and scattering from a vacuum-fired plume was proposed by Edwards et al.[9] In this model (PARRAD), eight parameters had to be specified to define the conical, axial, and radially varying plume, but parametric calculations showed that a wide choice of five of them gave almost the same engineering results; the three parameters that defined the Bobco model would often be sufficiently definitive. This engineering model for predicting heating neglected spectral variations and gas and soot radiation. Only alumina particles, treated as gray isotropic scatterers and emitters, were considered. The principal motivation for proposing the new heating model was to calculate angular variations of the plume boundary intensity since the validity of the diffuse radiosity assumption or some arbitrary angular corrections[10] was doubtful.

A number of questions about the base heating model remains. Could gas and soot radiation play a significant role in base heating radiation as Nelson[5] believes is the case in signature radiation? Since the model was proposed, new knowledge of the optical properties of alumina with impurities has been reported by Konopka et al.[11] with "...important implications for plume particulate emission models, such as that of Edwards and Bobco...." Do the new findings negate the model or require new input parameters? Does the neglect of spectral variations in the gray model require amendment? Can afterburning be accommodated so that the vacuum-firing SRM model can be applied to atmospheric firing motors? The objective of the present paper is to describe the basis for extending the previous model to include nongray gas, soot, and particulate radiation with three-dimensional spatial variations of temperature, pressure, and composition and to use the extended model to address these questions.

Alumina Particle Optics

Optical Constants

Malitson[12] recommended values of refractive index for alumina following the procedure of Sutton and Stavroudis[13]:

$$n_1^2(\lambda) - 1 = \frac{A_1\lambda^2}{\lambda^2 - B_1} + \frac{A_2\lambda^2}{\lambda^2 - B_2} + \frac{A_3\lambda^2}{\lambda^2 - B_3} \tag{1}$$

$$A_1 = 1.023798, \qquad A_2 = 1.058264, \qquad A_3 = 5.280792$$

$$B_1 = 0.00377588, \qquad B_2 = 0.0122544, \qquad B_3 = 321.3616$$

This fit of n_1 for solid alumina is used in the absence of information pertaining to liquid alumina. The fit indicates a drop in n_1 beyond 6 μm becoming quite steep near 10 μm. However, the total spectrum-integrated values of radiation from molten alumina are little affected by wavelengths beyond 6 μm and thus by uncertainty in any difference between liquid and solid alumina properties beyond that wavelength. Nevertheless, the thermophysics community would be well served by additional thermophysical property measurements of liquid alumina with and without impurities that are typical of solid rocket motors. The absorptive index is calculated according to Van de Hulst,[15]

$$n_2^2(\lambda,T) = (\varepsilon/2)[(1 + 4\sigma^2\lambda^2/c^2\varepsilon^2)^{1/2} - 1]$$

$$n_2^2(\lambda,T) = (\varepsilon/2)[(1 + \lambda^2/\lambda_\sigma^2)^{1/2} - 1] \tag{2a}$$

where by definition $\lambda_\sigma \equiv c^2\varepsilon^2/4\sigma^2$, and the electric constant is[12] $\varepsilon = 8.5$. The value of $\lambda_\sigma(T)$ was assigned based upon the value of $n_{2,0}(T)$ at $\lambda = \lambda_0 = 1.77$ μm. Rearranging Eq. (2)

$$\lambda_\sigma(T) = \lambda_0\{1 - [(2/\varepsilon)n_{2,0}(T) - 1]^2\}^{-1/2} \tag{2b}$$

The value of $n_2(T)$ was taken to vary with particle temperature T_p and molten fraction f_m in the manner proposed by Edwards and Bobco,[14] adjusted for the findings of Ref. 11.

$$n_{2,0}(T) = 3.56 \times 10^{-3}(1 - f_m)e^{(T_p - T_m)/2900} + 1.41 \times 10^{-3} f_m e^{(T_p - T_m)/492} \tag{3}$$

Figure 1 shows calculated values of $n_2(\lambda,T)$ resulting from Eqs. (2) and (3). Also shown are data from Ref. 11. A statement from Ref. 11 is repeated verbatim, "Obviously there can be no one 'good' set of Al_2O_3 rocket particle properties, at least in the solid phase, and the application of

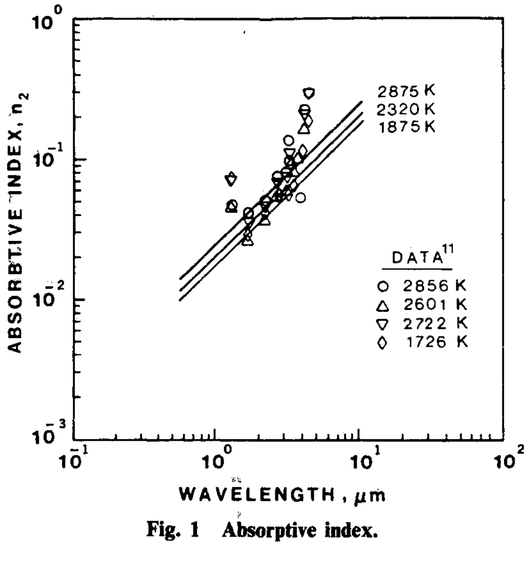

Fig. 1 Absorptive index.

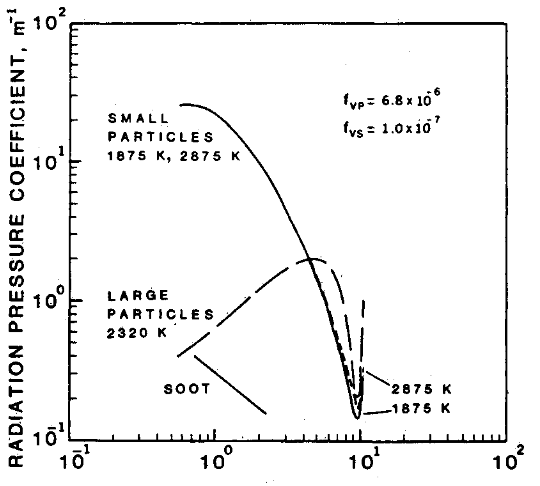

Fig. 2 Radiation pressure coefficient.

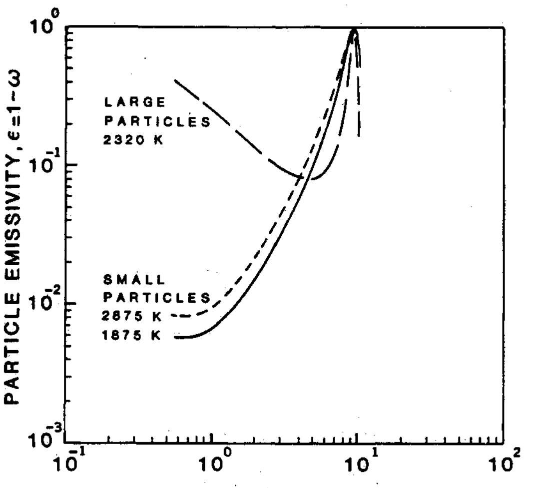

Fig. 3 Particle emissivity.

data obtained from one rocket engine to a different engine, or even to a different region in the nozzle exhaust of the same engine, should be viewed with extreme caution."

Effective Extinction and Albedo

Van de Hulst[15] gives approximate relations for extinction, absorption, scattering, and radiation pressure efficiencies as follows:

$$Q_{ex} = 2 + 4u^2\cos(2\beta) - 4\exp(-\rho\tan\beta)[u\sin(\rho-\beta) + u^2\cos(\rho-2\beta)] \tag{4}$$

$$Q_{abs} = 1 + (2/v)e^{-v} - (2/v^2)(1-e^{-v}) \tag{5}$$

$$Q_{pr} = Q_{ex} - \overline{\cos\theta}(Q_{ex} - Q_{abs}) \tag{6}$$

where

$$\rho = 2x(n_1 - 1) \tag{7a}$$

$$x = (2\pi r_p)/\lambda \tag{7b}$$

$$\tan\beta = n_2/(n_1 - 1) \tag{7c}$$

$$u = \cos\beta/\rho, \tag{7d}$$

$$v = 4xn_2 \tag{7e}$$

and

$$\overline{\cos\theta} = 0.07729x^2 + 1.3334x^3 - 0.05322x^4, \qquad x \le 2 \tag{8a}$$

$$\overline{\cos\theta} = 1 - 2.21919\exp(-0.78857x), \qquad x > 2 \tag{8b}$$

Equations (4–6) are valid and useful when $n_2 \ll n_1$ and $n_2 \ll 1$, and these conditions hold for aluminum oxide. The accompanying coefficient is obtained by integrating the efficiency over an assumed particle size distribution times the particle cross section. The distribution of Ref. 14 was employed for this purpose:

$$K_i(\lambda) = \frac{3}{2}\frac{nf_v}{D_0^2}\int_0^\infty \left(\frac{D}{D_0}\right)^{n-2} e^{-(D/D_0)^n} Q_i(D,\lambda)\,\mathrm{d}D$$

$$n = 2.5, \quad D_0 = 5.2\ \mu\text{m (large "hot" particles)} \tag{9}$$

Figure 2 shows $K_{pr}(\lambda)$ for $D_0 = 5.2\ \mu$m with $T_p = 2320$ K and $f_m = 0$. Also shown are curves for $D_0 = 0.5\ \mu$m with T_p = 1875 and 2875 K. Note the increasing K_{pr} with increasing λ up to 6 μm for the large particles. This behavior is just the opposite of that for the small particles. The difference in behaviors is primarily an interference effect brought about by the size-to-wavelength ratio multiplied by the refractive index n_1, which drops steeply in the vicinity of 10 μm. The absorptive index n_2 rises steadily over the wavelength range of concern.

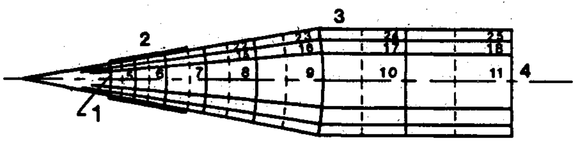

Fig. 4 Spatial grid.

Since the plumes of SRMs having a 10-cm or larger throat are scattering thick, an effective isotropic scattering model is appropriate.[16] For an effective isotropic scattering value of extinction, radiation pressure efficiency is appropriate.[17] The effective value for albedo and the particle emissivity are then

$$\omega(\lambda) = \frac{K_{pr}(\lambda) - K_{abs}(\lambda)}{K_{pr}(\lambda)} \tag{10a}$$

$$\varepsilon_h(\lambda) = 1 - \omega_h(\lambda), \qquad \varepsilon_{sp}(\lambda) = 1 - \omega_{sp}(\lambda) \tag{10b}$$

Figure 3 shows the particle emissivities corresponding to the curves in Fig. 2. Note again how the large-particle wavelength variation opposes those of the small particles. Again optical interference for the large particles, the decrease in n_1 near 10 μm, and the steady rise in n_2 explain the variation seen in the figure.

Model Description

Spatial Grid

The PARRAD code[9,18] originally provided for conical sides and spherical caps. Provision was made for cylindrical sides and planar ends beyond a conical section and for planes of constant azimuth, called "webs." A volume zone along the centerline was bounded by a conical or cylindrical side and two spherical end caps, or two planes of constant z, or one of each. Annular zones were bounded by two such conical or cylindrical sides and, not used here, azimuthal webs. The spatial domain was closed by an inner sphere, usually taken at the throat, a maximum cone half-angle or cylinder radius, and a maximum spherical radius or axial distance. The throat cap, nozzle wall (modeled as a cone), and "space" beyond the outer side or maximum axial station were assigned zone numbers and treated as blackbodies at appropriate temperatures. Figure 4 illustrates the mesh.

Particles

To the two sizes of alumina particles allowed by PARRAD was added soot. The submicron alumina particles were spread uniformly to the outer side boundaries and were taken to be "cold," i.e., at the local, axially varying gas temperature T_g. The larger alumina particles were confined, if desired, to an inner core and taken as "hot," i.e., possibly hotter than the local gas temperature. The hot particle temperature was either arbitrarily assigned or calculated from a spherical droplet cooling model with allowance for change of phase and Knudsen number effects. The soot was assumed to be "spread" and cold at the local gas temperature.

Spectral variations of the alumina particles were modeled in one of two ways. In one case an approximate expression was used for the spectral variations of the effective extinction coefficient and the particle albedo ω or emissivity $\varepsilon = 1 - \omega$. In the other case, the spectral variations were calculated using the Van de Hulst[15] approximations and the n_2 of Ref. 11 as explained in the preceding section.

The approximate expressions were taken in accord with Figs. 2 and 3. For hot large particles, the extinction coefficient and particle emissivity are

$$K_h(\lambda) = K_{h0}(\lambda/\lambda_0)^{+0.68} \tag{11}$$

$$\varepsilon_h(\lambda) = \varepsilon_{h0}(\lambda/\lambda_0)^{-0.68} \tag{12}$$

For hot small particles, when there is afterburning,

$$K_{sp}(\lambda) = K_{sp0}(\lambda/\lambda_0)^{-1.5} \tag{13}$$

$$\varepsilon_{sp}(\lambda) = \varepsilon_{sp0}(\lambda/\lambda_0)^{+1.5} \tag{14}$$

For cold, small particles

$$K_c(\lambda) = K_{c0}(\lambda/\lambda_0)^{-1.7}, \qquad \varepsilon_c = 0 \tag{15}$$

For soot, based upon the calculations of Tien and Lee[19] and measurements of Babikian et al.,[20]

$$K_s(\lambda) = K_{s0}(\lambda/\lambda_0)^{-0.8}, \qquad \varepsilon_s = 1 \tag{16}$$

Gas Radiation

The exponential band model was employed.[21] For an upper limit to gas radiation, the lines were assumed to be overlapped on the basis that hot bands (with upper vibrational states) fill in the vibrational-rotational line structure. This upper limit is a good approximation except perhaps for the HCl fundamental. For the one-sided kth band

$$K_{gk}(\nu) = (\alpha_k/\omega_k)\exp(-|\nu_{ck} - \nu|/\omega_k) \tag{17a}$$

or, if two-sided,

$$K_{gk}(\nu) = (\alpha_k/\omega_k)\exp(-2|\nu_{ck} - \nu|/\omega_k) \tag{17b}$$

where α_k is the integrated intensity and ω_k is the bandwidth parameter related to the rotational constant. For the gas mixture

$$K_g(\nu) = \sum_k K_{gk}(\nu) \tag{18}$$

The base-heated equipment was assumed to be sufficiently close so that atmospheric attenuation would be neglected. Again this assumption gives an upper limit.

Mixture Rules

At a given wave number, the total extinction coefficient is the sum of that from the small particles, large particles, soot, and gas. The total absorption coefficient is similarly summed. The mean effective blackbody emissive power is the absorption coefficient weighted sum

$$\bar{B} = \sum_i K_{ai} B_i \Big/ \sum_i K_{ai} \tag{19}$$

where B_i is the Planck function for the particle or gas temperature

$$B_j = \frac{2\pi h c^2 \nu^3}{e^{hc\nu/kT_j} - 1} \tag{20}$$

Source Function

Extinction coefficient, albedo, and B are volume-averaged for convenience

$$\bar{K}(\nu) = (1/V)\int K\,\mathrm{d}V \tag{21}$$

$$(1 - \bar{\omega})\bar{K} = (1/V)\int K(1 - \omega)\,\mathrm{d}V \tag{22}$$

$$(1 - \bar{\omega})\bar{K}\bar{B} = (1/V)\int K(1 - \omega)\,\bar{B}\,\mathrm{d}V \tag{23}$$

Then the fast-running hybrid Monte Carlo technique[9,22] is applied. The volume-to-volume shape factors are thus found using a 1000 or more Monte Carlo samplings that are rapidly computed accounting only for extinction. The 1000 Monte Carlo samplings give more accuracy than a two or six flux approximation. The plating algorithm[23] is applied to determine transfer factors, and the scattering/emitting source function is found by summing them. Multiple scatterings and inter-reflections are accounted for in converting the volume-to-volume shape factors into transfer factors via this technique. For example, the nozzle wall treated as black could easily be taken to be diffusely reflecting or reradiating. It is not necessary to store the spectral transfer factor matrix; only the spectral source function vector need be stored.

Once the spectral source function has been determined, fast-running line-of-sight calculations can be made to predict radiometer readings and heating rates.

Table 1 Definition of the nominal case

Nozzle	Exit radius, R_e	0.41 m
	Throat radius, R_t	0.22 m
	Cone angle, β	10 deg
	Wall temperature, T_w	1600 K
Plume geometry	Minimum z	2.34 m
	Cone-cylinder transition z	4.34 m
	Maximum z	7.11 m
Exit conditions[7]	Gas temperature, T_{ge}	1875 K
	Gas pressure, P_{ge}	1.7 atm
	Gas velocity, V_{ge}	2400 m/s
	Particle temperature, T_{pe}	2320 K
	Total mass flow rate, $\dot{m}_t$	361 kg/s
Exit mole fractions[7]	H_2	0.38
	CO	0.29
	HCl	0.12
	N_2	0.064
	CO_2	0.044
	H_2O	0.033
	Al_2O_3	0.069
Mixture properties	Molecular weight, M	18.608
	Specific heat ratio, γ	1.152
	Dynamic viscosity, μ, Ns/m^2	5.992×10^{-5}
	Thermal conductivity, k	0.285 W/m K
Particle optics	Equations (11–15)	
Radiative properties	Soot optical depth, t_{se}	0.35
	Small-particle optical depth, t_{spe}	10
	Large-particle optical depth, t_{he}	1
	Large-particle emissivity, ε_{he}	0.4
	Small-particle emissivity, ε_{spe}	0
	Emissivity decay exponent, n_h	1
	Source decay exponent, n_t	1

Table 2 Apparent radiosity viewed across the plume at two axial stations

Run		Variations from nominal case, nominal case in Table 1	πI [W/cm^2] $Z^* = 5.76$	πI [W/cm^2] $Z^* = 9.44$
1	Nominal case	——	62.6	22.0
2	Gray particles	Gray	62.6	22.4
3	No soot	$T_{se} = 0$	64.4	21.0
4	No soot or gas	$t_{se} = 0$, no gas	61.5	17.4
5	No alumina	$t_{hpe} = 0$, $t_{spe} = 0$	19.6	10.8
6	Gas only	$t_{se} = 0$, $t_{hpe} = 0$, $t_{spe} = 0$	11.6	5.4
7	Much cooler wall	$T_w = 800\,\mathrm{K}$	55.4	21.9
8	Cooler wall	$T_w = 1200\,\mathrm{K}$	57.2	21.9
9	Hotter wall	$T_w = 2000\,\mathrm{K}$	74.8	22.1
10	Much hotter wall	$T_w = 2400\,\mathrm{K}$	97.7	22.4
11	After burning	$\varepsilon_{spe} = 0.1$	112.0	81.3
12	Lower scattering	$\tau_{spe} = 5$	65.9	22.8
13	Much lower scattering	$t_{spe} = 2$	69.4	23.1
14	Less hot alumina	$t_{hpe} = 0.5$	49.7	17.2
15	Calculated particle optics and temperature	Particle optics Eqs. (4–10) T_p calculated, $\epsilon_{sp} > 0$	35.6	12.0
16	As run 15 with afterburning	As above with ϵ_{sp} calculated	88.8	75.8

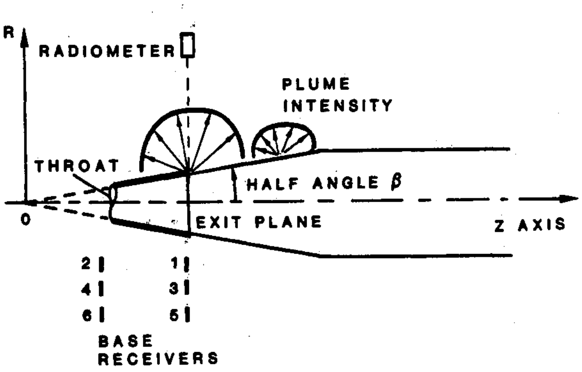

Fig. 5 Base receiver locations.

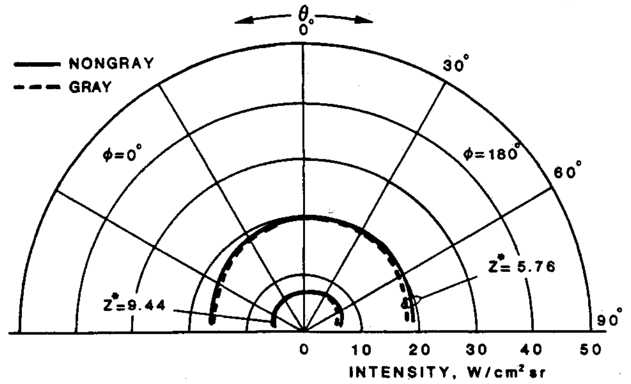

Fig. 6 Gray vs nongray behavior (see Tables 1 and 2 for conditions).

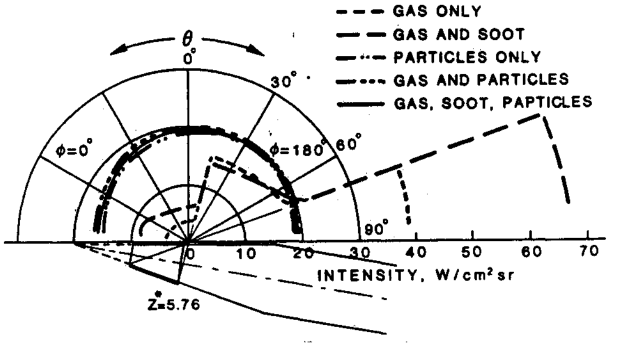

Fig. 7 Effect of radiating species (see Tables 1 and 2 for conditions).

Results

Base Case

Table 1 defines the base-case nominal values of large-particle optical depth, small-particle optical depth, gas composition, soot loading, nozzle and plume geometry, axial variations of optical depth, and large-particle emissivity and emissive power that were chosen. Calculations were made using 1024 Monte Carlo samplings per zone and 56 wave numbers. After the source functions were found, calculations were made to obtain directional distributions at two locations on the plume boundary ($Z^* = 5.76$ and 9.44 exit radii from the apex of an assumed 10-deg cone) and at six aft-facing receiver locations, as shown in Fig. 5.

Nongray Particle Radiation

Gray particle calculations using the properties at $\lambda_0 = 1.77$ μm as constant values throughout the spectrum were made for comparison with nongray particle radiation. The results of runs 1 and 2 in Table 2 show only a small difference, probably because the variations in K_h and ϵ_h give a constant product of the two, and the base-case small-particle optical depth is large. Shown in Table 2 are values of πI ($Z^* = 5.76$) and 3.68 radii down from it ($Z^* = 9.44$). The values are seen to be 62.6 and 22.0 W/cm^2 for the nongray case vs 62.6 and 22.4 W/cm^2 for the gray case. Figure 6 shows the intensity variation with polar angle θ for $\phi = 0$ (directed upstream) and $\phi = 180$ deg (directed downstream).

Gas and Soot Radiation

Comparisons of runs 1 and 3–6 show the effects of soot and gas radiation. Figure 7 shows the intensity directed fore and aft. If the gas contained no particulates, values of πI at the two locations are 11.6 and 5.4 W/cm^2. If soot is added in the amount assumed, the values become 19.6 and 10.8. Alumina alone contributes 61.5 and 17.4 W/cm^2. Alumina particles plus gas gives 64.4 and 21.0, whereas alumina plus soot plus gas gives 62.6 and 22.0 W/cm^2.

The values show that, unlike Nelson's[5] SIRRM calculations of signature, the gas and assumed soot have little effect upon the near-field radiation determining base heating. The bulk of the radiation is alumina particle radiation, and soot, if present, subtracts a little from it, partially offsetting what little the gas radiation adds.

Nozzle Wall Radiation

Nozzle wall radiation, as shown in runs 1 and 7–10 and in Fig. 8, shows a dramatic effect upon the exit radiosity but very little effect upon the downstream radiosity at $Z^* = 9.44$. As the wall temperature is varied from 800 to 2400 K, the exit radiosity climbs from 55.4 to 97.7 W/cm^2, nearly a factor of two. The downstream value of πI climbs only from 21.9 to 22.4 W/cm^2. The exit radiosity and apparent axial decay are affected greatly by a nozzle wall temperature above 1200 K.

Afterburning

As a crude indication of what effects plume boundary mixing and afterburning at sea level might have, the outer conical zones (zones 22–25 in Fig. 4) were assumed to be at core gas temperature plus 1000 K. The effects are dramatic. Not only does the exit radiosity in run 11 shoot up from 62.6 to 112.0 but the downstream radiosity leaps from 22.0 to 81.3 W/cm^2. Thus the calculated exit radiosity and the axial decay are profoundly affected.

Small-Particle Population

Depending upon the number of small particles in the plume, the scattering optical depth can be larger or smaller. The nominal case was $t_{spe} = 10$. Runs 12 and 13 show results for $t_{spe} = 5$ and 2, respectively. The plume radiosity climbs somewhat as t_{spe} drops. More dramatic, however, is the change in directional distribution of the plume intensity shown in Fig. 9. As t_{spe} drops, the intensity emerging from lines of sight penetrating upstream into the flow rises. The radiation directed upstream to the base region changes only 3.5% in the calculations shown in Table 3.

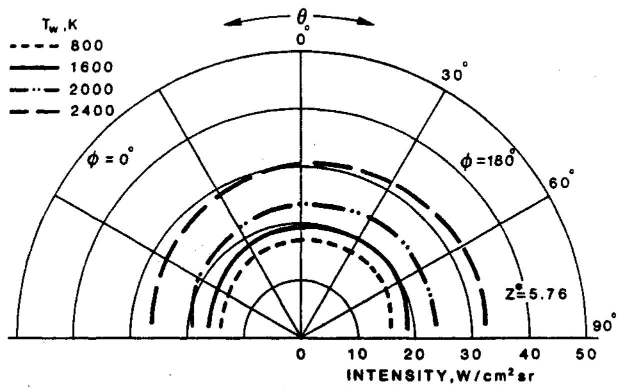

Fig. 8 Nozzle wall temperature effect (see Tables 1 and 2 for conditions).

Large-Particle Population

Varying the large-particle population has a significant impact, but the result is less than linear when the product of $\varepsilon_{he} K_{he}$ is 0.4. Runs 1 and 14 show that, as $\varepsilon_{he} K_{he}$ drops from 0.4 to 0.2, the exit radiosity drops from 62.6 to 49.7 W/cm^2. Figure 10 shows the corresponding intensity plots.

Particle Cooling

Rather than employ the fits in Eqs. (11–15) and the assumed ε_h and B_h axial decays, the spectral optics were calculated via Eqs. (4–10), and the particle temperature was calculated from heat-transfer considerations. Comparisons of

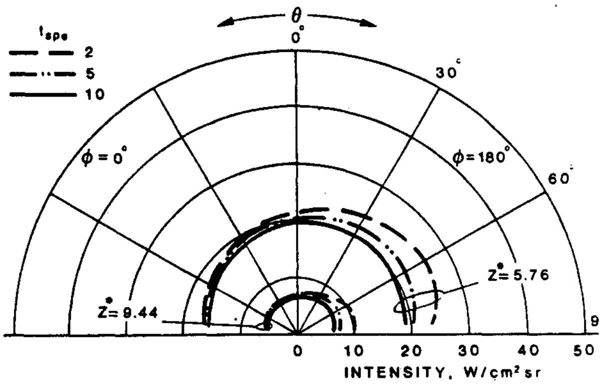

Fig. 9 Effect of small-particle optical depth (see Tables 1 and 2 for conditions).

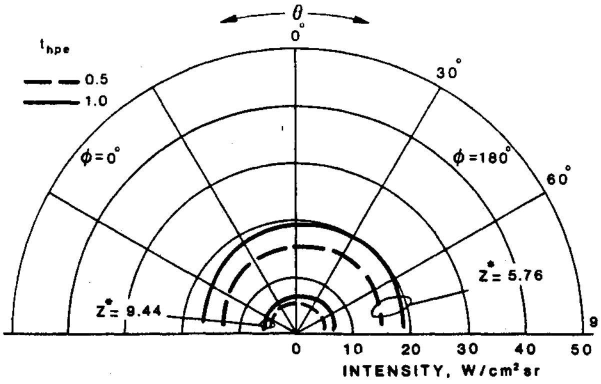

Fig. 10 Effect of hot particle optical depth (see Tables 1 and 2 for conditions).

Table 3 Irradiation of plume upon different receiver locations

Run		Irradiation, W/cm^2					
		R_1	R_2	R_3	R_4	R_5	R_6
1	Nominal case	2.55	0.53	1.35	0.54	0.81	0.52
2	Gray particles	2.54	0.41	1.34	0.53	0.81	0.51
3	No soot	2.55	0.41	1.32	0.53	0.78	0.51
4	No soot or gas	2.27	0.36	1.14	0.46	0.66	0.44
5	No alumina	1.14	0.25	0.64	0.29	0.39	0.26
6	Gas only	0.59	0.11	0.33	0.14	0.20	0.13
7	Much cooler wall	2.42	0.39	1.31	0.51	0.79	0.50
8	Cooler wall	2.46	0.40	1.32	0.52	0.79	0.50
9	Hotter wall	2.77	0.45	1.42	0.58	0.84	0.55
10	Much hotter wall	3.14	0.51	1.53	0.65	0.89	0.61
11	Afterburning	8.11	1.46	4.85	1.88	3.05	1.82
12	Lower scattering	2.60	0.42	1.38	0.54	0.82	0.53
13	Much lower scattering	2.64	0.43	1.40	0.56	0.83	0.54
14	Less hot alumina	1.97	0.32	1.04	0.42	0.63	0.40
15	Calculated particle optics and temperature	1.30	0.21	0.69	0.28	0.42	0.27
16	As run 15 with afterburning	8.06	1.46	4.72	1.84	2.86	1.74

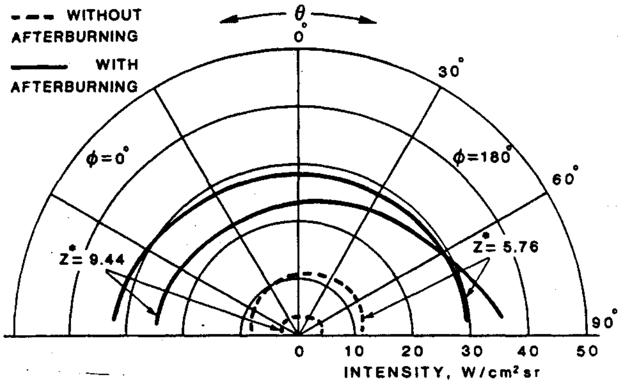

Fig. 11 Effect of afterburning according to the particle cooling model (see Tables 1 and 2 for conditions).

runs 1 and 15 show that the calculated exit radiosity drops to a low value not seen in test data for low expansion ratio boosters.[24] With afterburning, however, the results of the run 16 did not change in any essential qualitative manner from the calculated run 11 and did not greatly change quantitatively. Detailed examination showed that ε_{he} was 0.08 rather than the assumed 0.4 baseline value, and the optical depth t_{he} was greater since the product of $\varepsilon_{he} t_{he}$ had been kept constant in the comparison. The assumed values of large and small alumina particles required an 80-20 mass split, with 80% having a 5.2-μm mean diam in accord with Eq. (9) and 20% having a 0.5-μm diam. Figure 11 shows the intensity variation with and without afterburning.

Figure 9 does show that, if optical depth of the small alumina particles were to fall to as low as 2, marked changes in the directional distribution of the radiosity result.

Base Heating

Table 3 shows the base heating values for the runs tabulated in Table 2. Afterburning is indicated again as having a large effect on base heating. However, a vacuum-fired SRM may show a greater half-angle β than an atmospheric-fired SRM.

Discussion

The addition of nongray gas and soot radiation to PARRAD has little impact on base heating predictions as long as the alumina content of the SRM plume is appreciable. As long as the plume is scattering thick at the nozzle exit, base heating predictions are little affected by the nongrayness of the particle populations.

Prior to the findings of Konopka et al.[11] that frozen alumina containing impurities does have an appreciable absorptive index n_2, it was difficult to conceive that a rational model could explain the exit radiosity values of order 10^2 W/cm² observed.[24] One was tempted to speculate[9] that large particles pass through the throat and break up gradually in the supersonic section of the nozzle only just upstream of the exit and/or that they contained a fraction of unburned aluminum that would react with oxygen-bearing combustion products. With the n_2 data of Ref. 11, the uncoupled particle cooling calculation reported here indicates values of 36 W/cm² without afterburning and 89 W/cm² with it. It is now clear that a coupled two-dimensional particle cooling code (with heat from the cooling particles reheating the expanding gas and with the heavier particles remaining centrally concentrated due to their greater inertia against radial expansion) will predict even greater values, thus, approaching observations. A phenomenological model including afterburning needs to consider atmospheric entrainment and the resulting change in adiabatic flame temperature in the mixing layer. Such a model appears to be within reach.

Even if a realistic phenomenological model is achieved, a fast-running model such as PARRAD may continue to be of engineering use for predicting base heating. In view of the variability of SRM impurities drastically affecting particle optics (recall the quotation from Ref. 11), calculational models for base heating will continue to require empirical data for fine tuning. Table 4 lists a set of parameters to be used as a starting point in such tuning.

Table 4 Recommended starting point parameters for predicting base heating

Particle optics	Large-particle optical depth	$0.0125\dot{m}_p/R_e$
	Large-particle emissivity	0.15
	Small-particle optical depth	$0.125\dot{m}_p R_e$
	Small-particle emissivity	0.01
	Small-particle emissivity in the atmospheric mixing layer	0.02
	Emissivity decay exponent	1.0
	Source decay exponent	1.0
	Geometry decay exponent	1.0
Exit conditions	Large-particle temperature	2320 K
	Small-particle temperature in the atmospheric mixing layer	2900 K

References

[1] Ludwig, C. B., Malkmus, W., Freeman, G. N., Slack, M., and Reed, R., "A Theoretical Model for Absorbing, Emitting, and Scattering Plume Radiation," *Progress in Astronautics and Aeronautics: Spacecraft Radiative Transfer and Temperature Control,* Vol. 83, edited by T. E. Horton, AIAA, New York, 1982, pp. 11-127.

[2] Ludwig, C. B., Malkmus, W., Freeman, G. N., Reed, R., and Slack, M., "Infrared Radiation from Rocket Plumes," *SPIE Modern Utilization of Infrared Technology VI,* Vol. 253, 1980, pp. 122–128.

[3] Malkmus, W., and Reed, R., "Practical Treatment of Particle Plumes," *SPIE Modern Utilization of Infrared Technology VII,* Vol. 253, 1980, pp. 120–137.

[4] Nelson, H. F., "Influence of Particulates on Infrared Emission from Tactical Rocket Exhausts," *Journal of Spacecraft and Rockets,* Vol. 21, No. 5, 1984, pp. 425–432.

[5] Nelson, H. F., "Influence of Scattering on Infrared Signatures of Rocket Plumes," *Journal of Spacecraft and Rockets,* Vol. 21, No. 5, 1984, pp. 508–510.

[6] Lyons, R. B., Wormhoudt, J., and Kolb, C. E., "Calculation of Visible Radiation from Missle Plumes," *Progress in Astronautics and Aeronautics: Spacecraft Radiative Transfer and Temperature Control,* Vol. 83, edited by T. E. Horton, AIAA, New York, 1982, pp. 128-148.

[7] Lyons, R. B., Wormhoudt, J., and Gruninger, J., "Scattering of Radiation by Particles in Low-Altitude Plumes," *Journal of Spacecraft and Rockets,* Vol. 20, No. 2, 1983, pp. 189–192.

[8] Bobco, R. P., "Radiation from Conical Surfaces with Nonuniform Radiosity," *AIAA Journal,* Vol. 4, No. 3, 1966, pp. 544–546.

[9] Edwards, D. K., Sakurai, Y., and Babikian, D. S., "A Two-Particle Model for Rocket Plume Radiation," *Journal of Thermophysics and Heat Transfer,* Vol. 1, No. 1, 1987, pp. 13–20.

[10] Edwards, D. K., "Comment on Radiation from Conical Surfaces with Nonuniform Radiosity," *AIAA Journal,* Vol. 7, No. 8, 1966, pp. 1656–1659.

[11] Konopka, W. L., Reed, R. A., and Calia, V. S., "Measurements of Infrared Optical Properties of Al_2O_3 Particles," *Progress in Astronautics and Aeronautics: Spacecraft Contamination: Sources and Prevention,* Vol. 91, edited by J. A. Ronx and T. D. McCay, AIAA, New York, 1984, pp. 180-196.

[12] Malitson, I. H., "Refraction and Dispersion of Synthetic Sapphire," *Journal of Optical Society of America,* Vol. 52, No. 12, 1962, pp. 1377–1379.

[13] Sutton, L. E., and Stavroudis, O. N., "Fitting Refractive Index Data by Least Squares," *Journal of Optical Society of America,* Vol. 51, No. 8, 1961, pp. 901–905.

[14] Edwards, D. K., and Bobco, R. P., "Effect of Particle Size Distribution on the Radiosity of Solid Propellant Rocket Motor Plumes," *Progress in Astronautics and Aeronautics; Spacecraft Radiative Transfer and Temperature Control,* Vol. 83, edited by T. E. Horton, AIAA, New York, 1982, pp. 169-188.

[15] Van de Hulst, H. D., *Light Scattering by Small Particles,* Dover, New York, 1981, pp. 89–91, 127, 128, 179, 267–269.

[16] Brewster, M. Q., "Radiation-Stagnation Flow Model Aluminized

Solid Rocket Motor Internal Insulator Heat Transfer," *Journal of Thermophysics and Heat Transfer*, Vol. 3, No. 2, 1989, pp. 132–139.

[17] Condiff, W. D., "Anisotropic Scattering in Three-Dimensional Differential Approximation for Radiation Heat Transfer," *International Journal of Heat Mass Transfer*, Vol. 30, No. 7, 1987, pp. 1371–1380.

[18] Babikian, D. S., "Experimental and Computational Studies of Volumetric Radiation," Ph.D. Thesis, University of California, Irvine, 1989.

[19] Tien, C. L., and Lee, S. C., "Flame Radiation," *Progress in Energy Combustion Science*, Vol. 8, 1982, pp. 41–59.

[20] Babikian, D. S., Edwards, D. K., Karam, S. E., Wood, C. P., and Samuelsen, G. S., "Experimental Mass Absorption Coefficients of Soot in Spray Combustor Flames," *Journal of Thermophysics and Heat Transfer*, Vol. 4, No. 1, 1990, pp. 8–15.

[21] Edwards, D. K., and Balakrishnan, A., "Thermal Radiation by Combustion Gases," *International Journal of Heat Mass Transfer*, Vol. 16, No. 1, 1973, pp. 25–40.

[22] Edwards, D. K., "Hybrid Monte-Carlo Matrix-Inversion Formulation of Radiation Heat Transfer with Volume Scattering," *Proceedings of ASME 23rd National Heat Transfer Conference*, HTK-Vol. 45, ASME, New York, pp. 273–278.

[23] Edwards, D. K., "The Plating Algorithm for Radiation Script F Transfer Factor," *Journal of Heat Transfer*, Vol. 108, No. 1, 1986, pp. 237–238.

[24] Rader, R. J., Technical Specialist, Plume Effects and Contamination, Advanced Technology Development, McDonnell Douglas Astronautics, Huntington Beach, CA, personal communication, 1989.